Photocatalyst efficiencies in concrete technology: The effect of photocatalyst placement

CrossMark

Lu Yang[a,b], Amer Hakki[a], Fazhou Wang[b,*], Donald E. Macphee[a,*]

[a] Department of Chemistry, University of Aberdeen, Meston Building, Meston Walk, AB24 3UE Aberdeen, Scotland, United Kingdom
[b] State Key Laboratory of Silicate Materials for Architectures, Wuhan University of Technology, 122# Luoshi Road, Wuhan 430070, China

ARTICLE INFO

ABSTRACT

The application of photocatalysts in concrete technology is by now a well-established concept. However, despite the great opportunities for air quality improvements to be derived from the considerable concrete surfaces exposed to the atmosphere, particularly in cities where air quality is greatly affected by vehicle exhaust and industrial emissions, photocatalytic concretes are still not in mainstream application. With current levels of NOx pollution considerably exceeding EU legislative guidelines in urban centres throughout the industrialised world, it is important to consider what the issues are. The likely barriers to more widespread implementation are likely to include cost effectiveness, which needs to be related to photocatalyst impact, but the challenges in measuring impact on air quality directly are complex. This paper seeks to place photocatalytic efficiencies into context, comparing performances of the conventional photocatalyst dispersion in surface mortar coatings with that of photocatalysts supported on surface exposed aggregates. The nature and impact of catalyst binding to the aggregate is also discussed.

1. Introduction

There has been significant media attention in recent years on deteriorating air quality in urban environments. The negative health implications from airborne particulates and oxides of nitrogen (commonly expressed as NOx but mainly NO and NO$_2$), primarily from vehicle emissions, have become a global issue [1]; European Directives define the atmospheric concentration of NOx in ambient air to be at maximum of 40 μg/m^3 [2], while the actual concentration of NOx in almost all main European cities far exceeds this value, e.g., an hourly average of ca. 300 μg/m^3 (160 ppb) was reported in London (July 2017) [3]. The situation in China is even more extreme with NOx concentrations in large cities in the North China Plain (Beijing, Tianjin, most of Hebei, Henan, and Shandong provinces and the northern parts of Anhui and Jiangsu provinces) exceeding 450 ppb in July 2013 [4]. As an example of recent trends, NOx pollution in key UK populations centres (London and Edinburgh) are highlighted in Table 1 [3,5].

Photocatalysis has been associated in the scientific literature with NOx abatement for more than 20 years and photocatalytic concrete, as a photocatalyst support [6–18], has more recently been the subject of several significant research programmes [19,20] and the basis for commercial photocatalytic cements. However, despite the current and increasing air quality issues, photocatalytic concretes are still rarely

utilised in mainstream construction, their application being limited only to several site demonstrations in Italy [21], France [22], Japan [13,14], Belgium [23], United Kingdom [24], Netherlands [12], and China [25], etc.

A number of significant factors which limit photocatalytic efficiencies in cement-based systems have been previously summarised, e.g. [26], and some have been addressed, such as the use of surface treatments in improving photocatalyst dispersion [27,28]. In the present application, further significant efficiency advantages are derived from the separation of the photocatalyst chemistry from the interfering effects of cement chemistry [26,29] by supporting the photocatalyst onto a surface mounted aggregate (Fig. 1). Supported catalysis is a well-developed concept in offering improved exposure of the catalysts to reactants and is common in industrial catalytic technologies. In such a configuration however, the nature of the photocatalyst-support interactions is important. For durable performance, a strong chemical bond is necessary but the influence of bonding on photocatalytic mechanisms must be considered. This paper addresses these influences, specifically the efficiency of the photocatalytic process.

The barriers to more widespread implementation of photocatalytic concretes are likely to include cost and perhaps even a measure of scepticism as to their general effectiveness. The definition of photocatalyst efficiencies can represent a source of confusion; this is normally

Table 1
General trends towards NOx pollution in key populations centres of London and Edinburgh [3,5]

place	Parameter	NOx concentration ($\mu g/m^3$)						
		2010	2011	2012	2013	2014	2015	2016
London mean roadside	Average	135.9	136.6	150.6	148.3	147.3	140.2	155.3
	Maximum	241.1	268.1	280.0	265.3	298.2	275.7	335.8
Edinburgh St Leonard-s	Average	96.9	73.6	76.1	68.8	59.4	N/A	73.4
	Maximum	531	361	541	365	250	N/A	742

defined as the photonic efficiency and values of 0.01–1% are often quoted [30,31]. Since these numbers are normalised to the number of photons impinging on the photocatalyst, they do not readily convey the impact of the photocatalyst on moderating NOx concentrations. This paper places photocatalytic efficiencies into the context of the application by illustrating how photonic efficiencies translate into impacts on air quality, utilising comparisons between performances of photocatalysts, (i) conventionally placed, i.e. by incorporation into a surface mortar layer, and (ii) supported on surface exposed aggregates.

The photocatalytic treatment of NOx has been typically described as a sequential oxidation process. The higher the degree of NO and NO_2 conversion, the greater the catalyst activity.

$$NO \rightarrow HNO_2 \rightarrow NO_2 \rightarrow NO_3^-$$
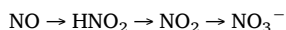
However, the photogenerated charge carriers on the catalyst can stimulate reduction as well as oxidation mechanisms so in practice, the reactions above may lead to intermediates in the above sequence being released to the atmosphere. This is problematic as the toxicity of NO_2 is considerably greater (by conservatively a factor of 3) than that of NO, the primary pollutant, and it can be a precursor for even more toxic atmospheric constituents, e.g. ozone and PAN (Peroxyacyl nitrates) [1,32,33]. Consequently, oxidation through to nitrate (NO_3^-) is the preferred reaction with respect to air quality.

The accumulation of NO_3^- on catalytic surfaces must however be managed; adsorbed NO_3^- blocks catalytic sites from further NO/NO_2 adsorption (and catalytic activity) and catalytic reduction back to NO_2 is likely, reducing nitrate selectivity. Therefore, NO_3^- must be removed regularly by washing. In conventional photocatalytic concretes, nitrate washings *via* condensed atmospheric moisture represents a mild risk from acidification of the cement (carbonated at the near surface) which may influence leaching induced damage over time. In the present configuration, the photocatalyst adsorbing and converting NOx to nitrate is supported on a quartz substrate mounted externally to the concrete and surface penetration of the concrete by acidified washings is less likely.

A measure of the effectiveness of the photocatalytic process in driving oxidation through to NO_3^- is given by the nitrate selectivity [31]. This property of TiO_2 is also addressed in the paper, particularly in the context of catalyst-support binding.
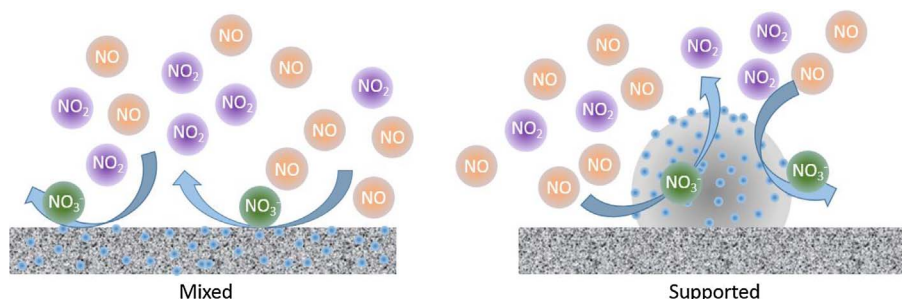
2. Experimental procedure

2.1. Materials

The aggregate used as a support in this study is ISO standard sand (ISO 679: 2009, quartz sand (LEUCATE, France), 1–2 mm diameter). Titanium tetra-isopropoxide (TTIP, 99.9%), acetic acid (CH_3COOH, 99.6%), Calcium hydroxide ($Ca(OH)_2$, 98%), absolute ethanol (C_2H_5OH, 99.9%), NaOH (sodium hydroxide, 0.1 M), were purchased from Sigma-Aldrich. Deionized water (18.2 MΩ.cm) was used throughout the preparation process.

2.2. Methods

2.2.1. TiO₂ hydrosol preparation

A low temperature precipitation-peptization method was employed to prepare anatase TiO_2 hydrosols as follows: 2.5 ml of TTIP was dissolved in 7.5 ml of absolute ethanol, with stirring for about 30 min at 50 °C. Then, the obtained solution was added dropwise into a mixture containing 2 ml of acetic acid and 40 ml of deionized water (1–2 drop/s). After that, the suspension was continually stirred for 48 h at 50 °C, and then aged for at least 72 h at room temperature to produce a translucent sol.

2.2.2. TiO₂/quartz sand aggregate preparation

A cyclic coating regime was employed to produce different loading levels of TiO_2 on the quartz sand surface. Specially, to maximize the surface hydroxide groups, the quartz sand aggregates were treated with 0.1 M NaOH for 24 h followed by washing with deionized water 3 times prior to immersion in the anatase TiO_2 hydrosols suspension; 1–2 mm alkaline treated quartz sands were immersed in anatase TiO_2 hydrosol suspensions for 5 min at room temperature. The resulting composites were then separated by filtration and dried at 105 °C for 30 min. This process was repeated for the required number of coating cycles. In the final step, all samples were dried at 105 °C for 24 h, then washed three times using deionized water before final drying at 105 °C for 24 h. These samples are labelled QST-X, where X is the number of coatings (X = 0, 1, 2, 3, 4, 5, 6).

2.2.3. Durability of coatings – evaluation methods
2.2.3.1. Mechanical.
The mechanical durability of the QST aggregates (TiO_2-loaded quartz composites) was evaluated using two methods [34]. Method 1:15 g QST aggregates were immersed in 30 ml deionized water and gently shaken manually for ca.15 s. The water was replaced and the process repeated for up to 30 cycles. Method 2: QST aggregates were immersed in deionized water, and then sonicated for 10 min, using a Branson ultrasonic bath (B300, 34 kHz, 50 W), after which it was washed with deionized water several times until a clear solution was observed.

2.2.3.2. Chemical.
The influences of cement chemistry were tested on the aggregate-supported catalyst system as follows:

Fig. 1. Conventional (mixed) and aggregate-supported configurations for photocatalyst (blue) applications in concrete technology. (For interpretation of the references to colour in this figure legend, the reader is referred to the web version of this article.)

Mixed

Supported

(1) QST-X aggregates were immersed in saturated aqueous $Ca(OH)_2$ solution for 1, 5, 10 and 30 min. The wet sample was then placed in a vacuum oven (105 °C; 4 h at 0.1 MPa), after which it was placed in a sample bottle and stored in a desiccator to await testing and designated (QST-X-Ci, Ci (i = 1, 5, 10, 30) represents $Ca(OH)_2$ attacking time). A QST-X was alternatively immersed in 0.1 M NaOH for 24 h, and then washed to neutral condition (denoted as QST-X-N);

(2) Carbonation − the above QST-X-Ci aggregates were placed in a flowing atmosphere containing 100% CO_2 (BOC U1013) at a relative humidity of 70% 1 h (flow rate: 5 ml/min), before being placed in a sample bottle and stored in a desiccator to await testing and designated QST-X-CiC (CiC represents QST-X-Ci being carbonated).

2.3. Characterization

The phase compositions of TiO_2 and QST were determined by comparing X-ray diffraction (XRD) patterns, obtained on a PHILIPS P W 3O4O/60X' PertPRO diffractometer in the range 20–70° 2θ under Cu Kα radiation at a scanning speed of 6° min^{-1}, against reference XRD data.

Fourier transform infrared (FT-IR) spectra were obtained using a Perkin-Elmer Spectrum 2 spectrometer with 48 scans per sample collected from 400 to 4000 cm^{-1} at 2 cm^{-1} resolution. The obtained FT-IR spectra were deconvoluted using Peakfit V. 4.1.2 software [35], and the concentrations of the chemical linkage Si-O-Ti, relative to SiO_2 and TiO_2 were calculated by the following formula [36]:

$$D_{(Si\text{-}O\text{-}Ti)} = \frac{S_{(Si-O-Ti)}}{S_{(Si-O-Si)}} \times \frac{X_{Si}}{X_{Ti}} \tag{1}$$

where $D_{(Si\text{-}O\text{-}Ti)}$ represents the concentration of Si−O−Ti bonds relative to Si−O−Si, normalized to the TiO_2/SiO_2 molar ratio; $S_{(Si-O-Ti)}$ and $S_{(Si-O-Si)}$ represent the background-corrected areas associated with the Si−O−Ti (ca. 940 cm^{-1}) and Si−O−Si (ca. 1170 cm^{-1}) absorption frequencies, respectively; x_{Si}/x_{Ti} represents the SiO_2/TiO_2 molar ratio, obtained by quantitative X-ray fluorescence (XRF, Rigaku $NEXQC^+$) calibrated using TiO_2-quartz sands mixtures in the range 0.1–50 wt.% TiO_2. The estimated error in $D_{(Si−O−Ti)}$ is around ± 6% [35].

Morphologies of samples were observed by scanning electron microscope (SEM, Zeiss EVO MA10) equipped with an energy dispersive x-ray spectrometry (EDS, Oxford INCA) for elemental composition analyses.

The theoretical loading thickness of TiO_2 film on quartz sand aggregate surface was calculated based on the model illustrated in Fig. 2 [34,37] and Eqs. (2) and (3):

$$\omega\% = \frac{\left(\frac{D_{st}}{D_s}\right)^3 - 1}{\frac{6 \times \rho_s}{\pi \times \rho_t} + \left(\frac{D_{st}}{D_s}\right)^3 - 1} \times 100 \tag{2}$$

$$d = \frac{D_{st} - D_s}{2} \tag{3}$$

Where ρ_s is the density of support, 2.4 g/cm^3; ρ_t is the density of TiO_2,

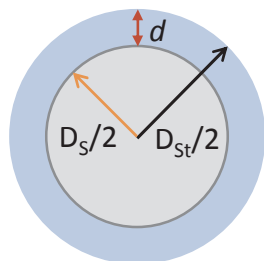**Fig. 2.** Geometric model for evaluating loading thickness of TiO_2 on aggregates and definition of parameters.

3.8 g/cm^3; D_s is the average diameter of support, nm; D_{st} is the average diameter of TiO_2 loaded support, nm; $\omega\%$ is the mass fraction of TiO_2 measured by XRF; d is the thickness of loaded TiO_2 film, nm. The model assumes that the coating layer consists of two dimensional closed packed spherical particles fully covering the smooth aggregate surface, with successive layers contributing to the thickness, d.

2.4. Photocatalytic performance

The photocatalytic performance of prepared samples were identified in a flow-through reactor (ISO 22197-1: 2007) schematically illustrated in Fig. 3.

10 g of QST aggregates were uniformly distributed in a rectangular recess (monolayer distribution, area 5×10^{-3} m^2) inside the reactor so the NO gas had to flow over the sample surface. The sample was irradiated by a 500W Xe-lamp solar illuminator (Sciencetech. Inc, Canada) light source; the resulting photon flux at the position of the sample was measured to be 3.05×10^{-6} mol s^{-1} m^{-2} using a broadband thermopile detector (Gentec-EO-XLP12-3S-H2-D0). 1 ppm of NO gas in synthetic air, conditioned at a constant 40% relative humidity, measured using a HygroPalm 1 detector (Rotronic) at 25 °C, was passed at a volumetric flow rate of 5×10^{-5} m^3 s^{-1} through the reactor. The concentrations of NO, NO_2 and NOx were detected by a Thermo Scientific Model 42i-HL High Level NO-NO_2-NOx Analyzer (Air Monitors Ltd., United Kingdom). Each sample was measured in the dark until equilibrium concentrations were reached and afterwards, under illumination, until steady state concentrations were observed. For comparison, the photocatalytic performance of pure TiO_2 (0.1 g), obtained by drying the TiO_2 hydrosol at 105 °C for 24 h, was measured under identical conditions. Kisch and Bahnemann [38] showed extended NOx experiments on a commercial TiO_2 photocatalyst which indicated that steady state conditions were reached 2 h after illumination. Consequently all concentrations for subsequent calculations of photonic efficiency and selectivity were extracted 2 h after illumination. The photocatalytic efficiency (ξ) was calculated according to Eq. (4). The catalyst selectivity for nitrate (S%) was calculated according to Eq. (5).

$$\xi = \frac{(c_d - c_i)VP}{\Phi ART} \tag{4}$$

$$S\% = \frac{\xi_{NO_X}}{\xi_{NO}} \times 100 \tag{5}$$

Where c_d is the concentration in dark, c_i the concentration under illumination, V the volumetric flow rate, p the pressure, A the irradiated sample area, R the gas constant, T the absolute temperature and Φ the photon flux impinging the photocatalyst surface. The photocatalytic efficiency was determined separately for NO, NO_2 and total NOx.

3. Results and discussion

3.1. Physical and chemical properties

The XRD pattern of the prepared TiO_2 shows the sample was well-crystallised anatase (Fig. 4). TiO_2 loaded onto quartz in the QST composites was of insufficient quantity to appear in the composite powder patterns but XRF results, shown in Table 2, confirm that the TiO_2 loading increases with the number of coating cycles as expected. This translates to loading thicknesses (d) of up to 1850 nm at a TiO_2/SiO_2 mass fraction (MF) of 0.61%. It can be concluded that the coating method produces TiO_2 multilayers. These represent agglomerates derived from individual TiO_2 nanoparticles; these represent agglomerates derived from individual TiO_2 nanoparticles; XRD data (peaks corresponding to (101) and (200)) and the Scherrer equation give a mean crystallite size of 10.3 ± 0.2 nm.

As shown in Fig. 5, the semi-quantitative FT-IR technique with peak deconvolution was used to characterise the TiO_2-SiO_2 binding in the
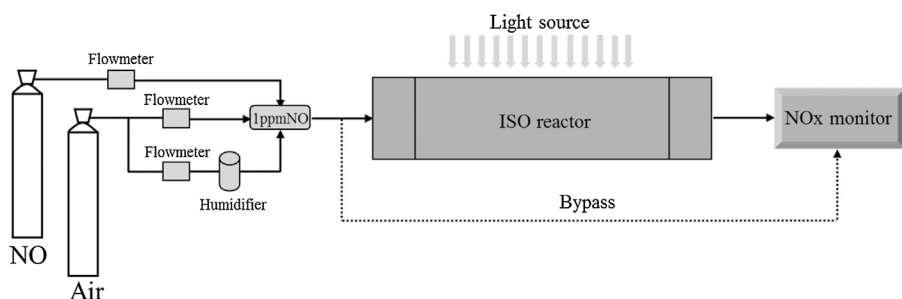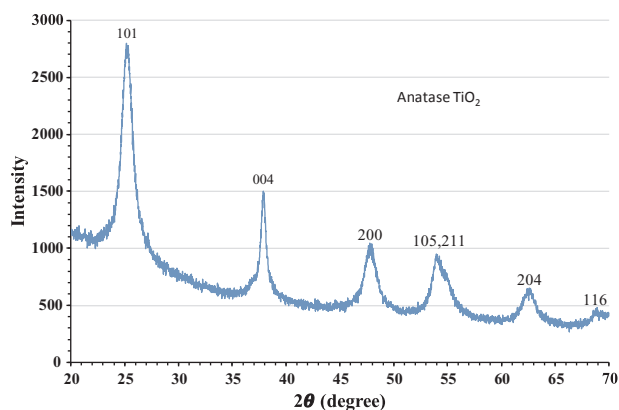
Fig. 4. Indexed XRD pattern of prepared TiO2 hydrosols dried at 105 °C.

Table 2

TiO2 loading average mass fraction (%) and average thickness (nm) on quartz sand aggregates surface with different coating times.

Sample	QST-0	QST-1	QST-2	QST-3	QST-4	QST-5	QST-6
MF[a]/%	–	0.16%	0.20%	0.31%	0.37%	0.46%	0.61%
d[b]/nm	–	480	620	940	1140	1400	1850

[a] Mass fraction, obtained by XRF measurement with calibration.

[b] Thickness, calculated by formulae (2) and (3) using measured mass fraction; QST-X represents X cycle coating times (X = 0, 1, 2, 3, 4, 5, 6).

QST-X composites. Fig. 5(a) presents a typical FT-IR spectrum (in this case, QST-2 (0.2% TiO2 mass fraction)) in the range of 650–1350 cm^{-1}. The equivalent spectrum for quartz is also shown. The absorption bands at 695, 778, 797, 1062, 1085, and 1165 cm^{-1} are associated with Si−O−Si bonds [39–42]. The broad absorption in the range of 850 − 1000 cm^{-1} is attributed to Ti−O−Si chemical linkages between the support and TiO2 particles [30]. It is reported that the broad peak in the range of 800–1350 cm^{-1} can be deconvoluted into five peaks [36,43,44] as shown in Fig. 5(b). The deconvoluted peaks at ca. 1066, 1088, 1117, and 1171 cm^{-1} are associated with the symmetric and asymmetric vibrations of Si−O−Si bonds, and the deconvoluted peak at ca. 940 cm^{-1} is attributed to Si−O−Ti bonds. The best separation of Si−O−Si peaks from the Si−O−Ti peak is achieved with the Si-O-Si absorbance at 1170 cm^{-1} so this peak was subsequently used in calculation of (Ti−O−Si)/(Si−O−Si) concentration ratios. When plotted against the mass fraction of TiO2 in each composite, Ti-O-Si/Si-O-Si area ratios present similar values (Fig. 6), indicating similar levels of Ti−O−Si bonding on quartz surfaces in all samples irrespective of TiO2 loading. This is consistent with a TiO2-saturated aggregate surface across the TiO2-loading range. As TiO2 loading increases, multi-layer (agglomerated) TiO2 increases (Ti−O−Ti) but does not affect the level of interfacial bonding. Nevertheless, this effect dilutes the effects of Ti−O−Si linkages (decreasing (D$_{(Ti−O−Si)}$)).
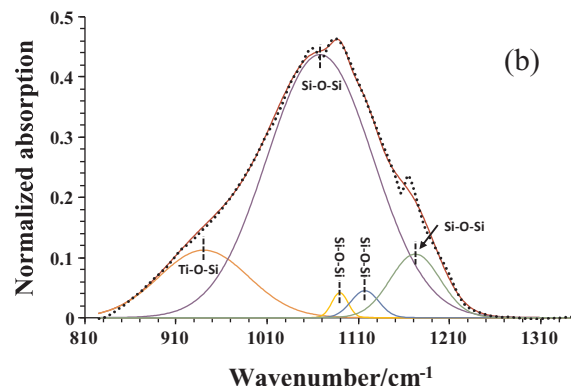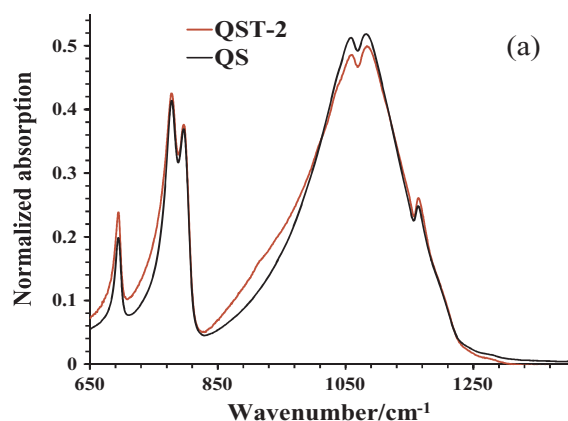

Fig. 5. Representative FT-IR spectra of (a) QS (aggregate) and TiO2-loaded aggregate (QST-2; 0.20% TiO2 mass fraction), and (b) QST-2 with component peaks identified by deconvolution in the wavenumber range 825–1350 cm^{-1}.
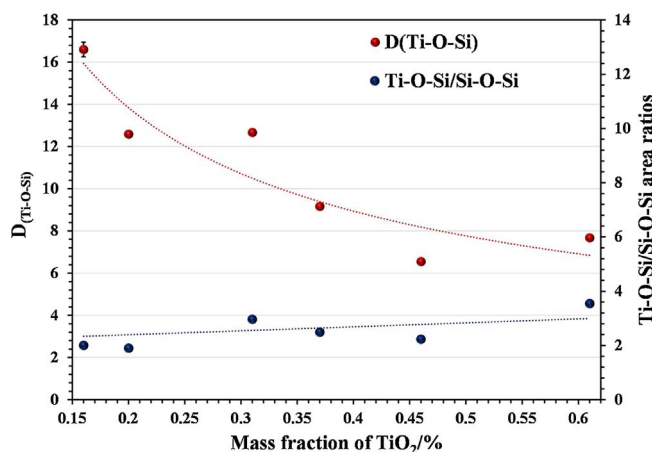

Fig. 6. Variation in Ti−O−Si/Si−O−Si area ratios and D$_{(Ti−O−Si)}$ with TiO2 loading on QST−X composites.
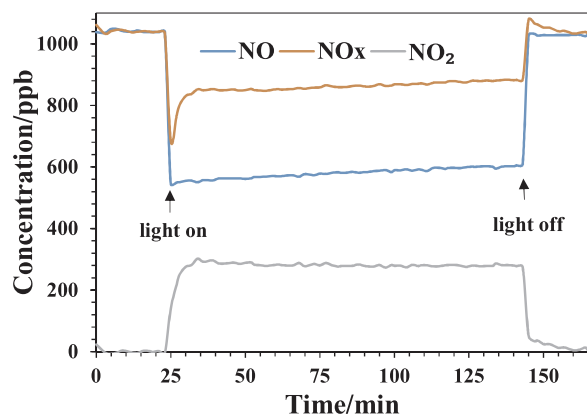
Fig. 7. Concentration profiles for NO, NO_2 and NOx (NO + NO_2) during the photo-catalytic oxidation of NO on TiO_2 hydrosol (0.1 g) photocatalysts.

Fig. 9. The dependence of nitrate selectivity and $D_{(Si-O-Ti)}$ on TiO_2 loading thickness for QST−X samples.

3.2. Utilization efficiencies of supported TiO_2

A typical concentration profile observed for the prepared TiO_2 sample during the photocatalytic oxidation of NOx on TiO_2 photo-catalysts is shown in Fig. 7. Three stages can be identified: 1) NOx concentrations stabilization without light illumination, 2) NOx photo-catalytic reaction with light on, 3) NOx concentrations recovery after turning off the light. NO concentration decreases rapidly upon sample illumination, and remains almost constant, while NO_2 concentration increases significantly at the same time. When the light is switched off, NO_2 concentrations decrease to zero. The photonic efficiency (ξ) of NO, NOx removal and NO_2 intermediate production, as well as the nitrate selectivity (S%) for all QST samples with different TiO_2 mass fractions are shown in Fig. 8. It can be noted that ξ (NO) increased initially with increasing TiO_2 mass fractions but became steady around 0.76%. At the same time, the ξ (NOx) and S% also increase with increasing the mass fraction of TiO_2 which drives a corresponding decrease of NO_2 pro-duction rate. Compared with the NOx removal results for pure TiO_2 (Fig. 7), the calculated values according to Eqs. (4) and (5) are ca. 0.6% for ξ (NO) and ca. 40% for nitrate selectivity, whilst the supported TiO_2 particles present higher photonic efficiency for NO removal, but lower nitrate selectivity (due to reduced NO_2 removal efficiency).

The detrimental influence of the Ti−O−Si linkage on selectivity has already been reported [45] but in this case, an increase in S% with TiO_2 loading fraction can be observed. This is still consistent with our earlier findings [30,45]. Where TiO_2 loading on SiO_2 is increased, the con-centration of Ti−O−Si, which is located only at the catalyst-support interface, with respect to Ti−O−Ti, is diluted by the multi-layer TiO_2 'coating', thus reducing the negative impact of the TiO_2-SiO_2 bonded interface and enabling S% to increase as is shown in Fig. 9. Further, the
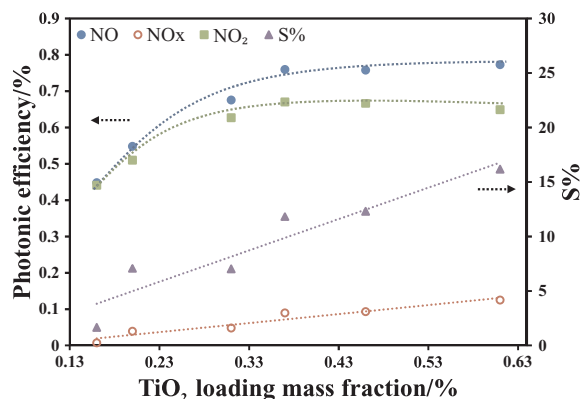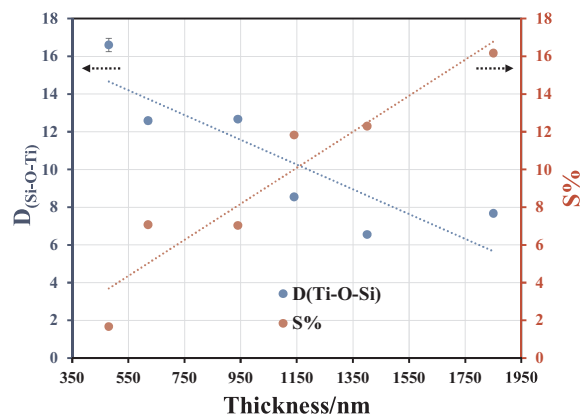
general shape of the ξ (NO) *vs* TiO_2 loading mass fraction profile in Fig. 8 is consistent with that observed earlier utilising smaller aggregate sizes [27]. In this case, the variation in ξ (NO) as TiO_2 loading increases was correlated almost perfectly with the trend in BET surface area (see Fig. S1), suggesting the importance of an *effective* surface area of TiO_2, probably influenced by particle packing in the multi-layer agglomer-ated structures.

3.3. Durability of supported TiO_2

3.3.1. Mechanical

The stability of TiO_2-aggregates composites is very important to the real engineering applications for long-term degradation of pollutants. Fig. 10 presents durability data for QST subjected to water washing. With gentle agitation, 30% of TiO_2 was removed after 10 cycles, however, only a further ca. 6% was lost after between 10 and 30 cycles. By comparison, after 10 mins sonication (SW10), ca. 56% of the TiO_2 loading remained. In both cases, a strong adhesion is indicated in the inner part of the composite, with weaker (outer) attachments being broken at higher loadings (greater distances from the bonded interface). Quantitative FT-IR data support this, showing constant Ti-O-Si/Si-O-Si area ratios throughout the durability test (See Fig. 10).

Coating TiO_2 onto quartz can be observed in Fig. 11 which shows complete TiO_2 coverage (Fig. 11(b)) compared with the uncoated quartz (QS) (Fig. 11(a)). Fig. 11(c) (and spectrum 3) shows that TiO_2 is still associated with the support even after sonication and washing, although at reduced level, as indicated by Spectrum 3 and the FTIR data.

Fig. 12 shows the photonic efficiency and nitrate selectivity of QST-6 and washed QST-6 samples with different washing cycles and re-gimes. It is noted that the washed QST samples present slightly different De-NOx performances (0.65–0.78% ξ (NO)) and nitrate selectivity

Fig. 8. The dependence of NOx photonic efficiency and nitrate selectivity of QST-X samples on TiO_2 loading mass fraction.
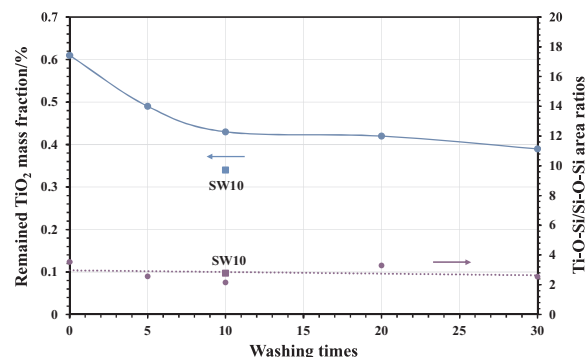

Fig. 10. Adhesion durability of QST-6 (0.61% TiO_2); SW10 indicates 10 min ultra-sonication followed by water washing to clear supernatants.
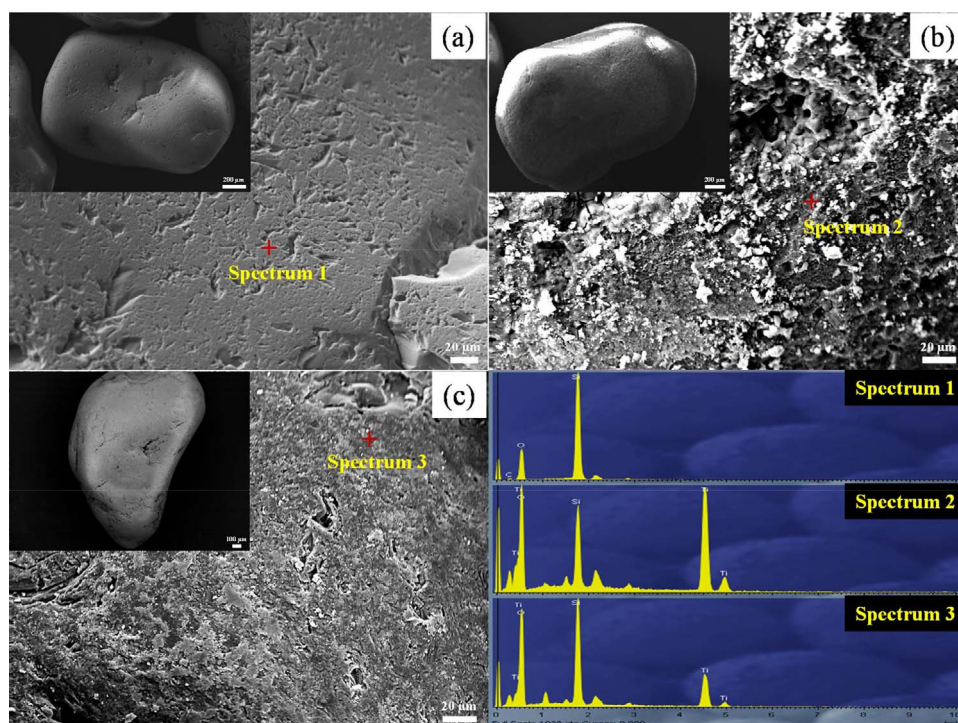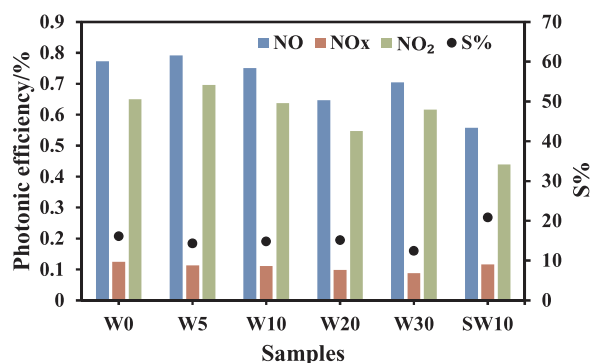
Fig. 12. Photonic efficiency and nitrate selectivity of QST-6 (0.61% TiO_2 mass fraction) and washed QST-6 samples (with reduced TiO_2 mass fraction) as a function of washing cycles and regimes.

(12%–15%). Even after the more aggressive sonication/washing treatment (SW10), the ξ (NO) photonic efficiency is only reduced by 30% even though almost half of the TiO_2 has been lost (0.34% remaining; Fig. 10). The greater selectivity of SW10 relative to W10 (Fig. 10) presents an apparent contradiction, i.e. the higher nitrate selectivity seems to be associated with a reduced TiO_2 layer thickness, contrary to the trend of Fig. 9. However, *accessible* surface area is believed to be important and it is suggested that the increased agitation from sonication has exposed more TiO_2 surface, increasing the degree of surface water on TiO_2. This has previously been shown to increase nitrate selectivity on TiO_2 [30]. The reduced ξ_{NO} may be attributed to reduce NO adsorption due to competition with water whilst NO_2 oxidation is enhanced in the presence of physi-sorbed water [30].

More significantly, this performance, which is achieved with approximately 34 mg of TiO_2 is similar to that of pure TiO_2 (0.1 g), confirming that supported TiO_2 has greater utilization efficiency, corresponding to a considerably lower cost of use in photocatalytic concrete.

3.3.2. Chemical

The influence of the chemical environment in cements (alkali, Ca substances, CO_2, etc.) must also be considered for real photocatalysis

applications [15,26,46–54]. We have recently reported positive correlations between photocatalytic performance and alkalinity during TiO_2 preparation/conditioning [30] so the QST composites were subjected to immersion in freshly prepared saturated $Ca(OH)_2$ solution. Fig. 13 shows SEM/EDS data for QST-6 after 30 min immersion (QST-6-C30). Also shown are data for the same material subsequently exposed to 1000 ppm CO_2 at 70% RH for 1 h (QST-6-C30C).

It can be observed that the morphologies of both samples are similar to those shown in Fig. 13 and indicate that there is still a deposited TiO_2 layer on the quartz surface, also confirmed by XRF measurement (0.5% TiO_2 mass fraction). The EDS data of Fig. 13(a) confirm the incorporation of Ca in the layer, presumably due to $Ca(OH)_2$ deposition, although at the resolution shown there is no specific morphological confirmation. In alkaline conditions, the negative surface charge on TiO_2 may be a factor in encouraging $Ca(OH)_2$ association, *via* the δ + charge on Ca. A similar interpretation can be offered for the QST-6-C30C sample, where carbonation of the deposited $Ca(OH)_2$ must be assumed. In either case though, the TiO_2 layer seems to have been sustained and its photocatalytic performance appears to have improved after exposure to $Ca(OH)_2$ (Fig. 14). This is an interesting observation as the enhancement of nitrate selectivity (S%) is particularly important. It is not clear why such an improvement should be associated with Ca but the earlier mentioned relationship with the effects of alkalinity on activating the TiO_2 surface is likely to be responsible, as supported by the example with NaOH treatment. A further factor is the positive role of surface adsorbed water in conditioning nitrate selectivity of TiO_2 [30], also induced by alkaline hydrolysis of the TiO_2 but which may also be enhanced by the presence of the hydrophilic $Ca(OH)_2$.

These effects appear to be slightly inhibited upon carbonation (Figs. 13 and 14). In fact, the reduction in alkalinity arising from carbonation may be a factor but also, it is less hydrophylic than $Ca(OH)_2$ and therefore less likely to favour an enhancement in water adsorption. The residual enhancements observed in the QST-6-CiC series are therefore likely to be due to uncarbonated $Ca(OH)_2$.

The negative effects of Ca additions on supported TiO_2 are mainly associated with activity. A decrease in ξ (NO) from 0.78% to 0.41% in the first 5 min of $Ca(OH)_2$ exposure (QST-6-C5) can be noticed in Fig. 14. It then becomes steady, indicating some competing influence
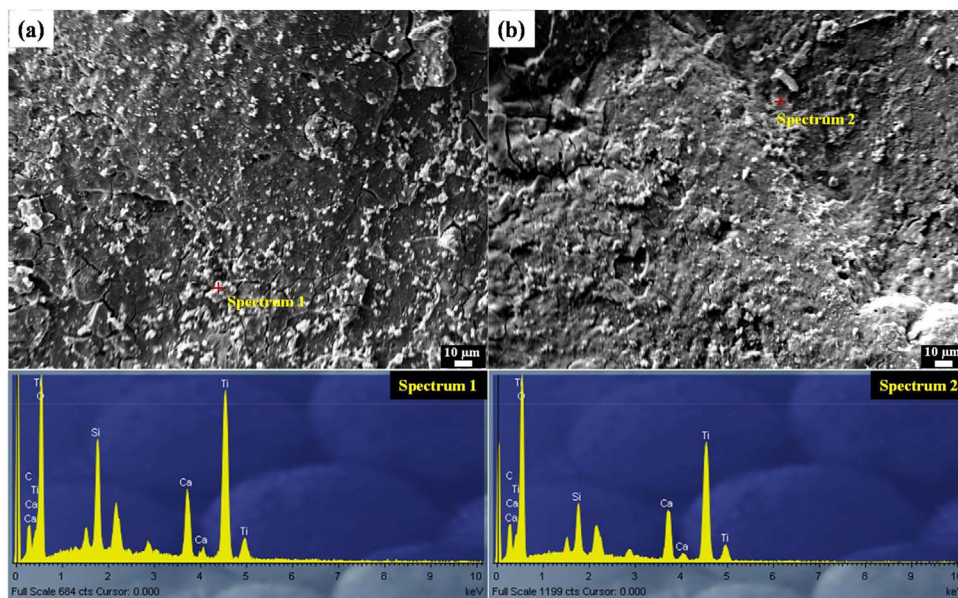
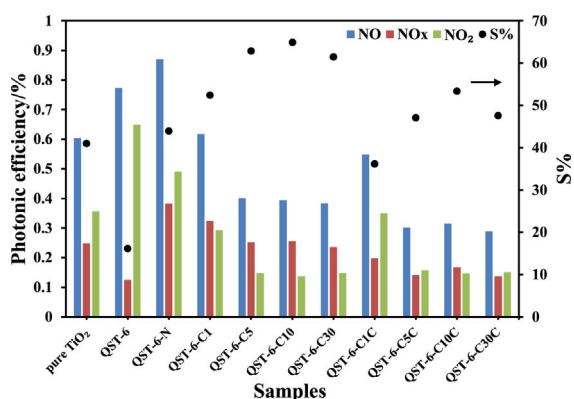**Fig. 13.** SEM images and EDS elements spectra of: (a) QST-6-C30; (b) QST-6-C30C.

Fig. 14. Photonic efficiency and nitrate selectivity of pure TiO$_2$ and QST-6 (0.61% TiO$_2$ mass fraction) under different exposure conditions.

but it is unlikely to represent TiO$_2$ film saturation which would be expected to reduce ξ (NO) to zero. A similar trend is observed for the carbonated sample but again, this may be attributed only to the reduced availability of Ca(OH)$_2$.

3.4. Opportunities for implementation

A basis for translating the photonic efficiency into quantifiable impacts on air quality in a real-life context may be modelled from data gathered using a photocatalytic reactor consistent with ISO 22197-1:2007. Rearrangement of Eq. (4) enables the photocatalyst-modified concentration, C_i, to be calculated from the photonic efficiency defined under laboratory conditions (Eq. (5)); NO is chosen for this illustration but NOx and NO$_2$ can be similarly treated.

$$C_i = C_d - \frac{\xi(NO)\Phi ART}{VP} \quad (5)$$

C_d represents the concentration measured over a non-illuminated area, expected to represent the equivalent of the concentration over a non-photocatalytically treated (reference) area; ξ(NO) represents the laboratory determined photonic efficiency of the photocatalyst. Other terms in Eq. (5) are previously defined, except for Φ and V. The UV irradiation intensity (Φ), is calculated according to Ref. [55] for noon on each day over a 1 year period (see Fig. S2). The model in ref [55] produces Φ in units of W m^{-2} and conversion to moles of

photons.m^{-2} s^{-1}, as required in Eq. (5), is by application of Eq. (6).

$$\Phi(mols. \, photons/m^2. \, s) = \Phi(W/m^2) \times \frac{\lambda}{N_A \times h \times c} \quad (6)$$

where λ is the wavelength (taken as 3.65 × 10^{-7} m), N$_A$ is Avogadro's number, h is Planck's constant (6.63 × 10^{-34} J.s) and c is the velocity of light (2.998 × 10^8 m.s^{-1}).

The volumetric flow rate (V, $m^3 s^{-1}$), is calculated from ambient wind speed v ($m\,s^{-1}$) corrected according to the height (distance) from the photocatalytic surface. In this case, Eq. (5) utilizes a value for ξ(NO) derived from measurements in which the air volume above the photocatalyst had a maximum height of 5 mm so recorded wind speeds measured at height h can be adjusted to that at 5 mm using Eq. (7); the results are shown in Table S1:

$$v_w(h) = v_{10} \times \left(\frac{h}{h_{10}}\right)^a \quad (7)$$

where v_w (h) is velocity of the wind ($m\,s^{-1}$), at height h; v_{10} is velocity of the wind ($m\,s^{-1}$), recorded at height h_{10} = 10 m; a is Hellmann exponent, which depends on the location and the shape of the ground; for unstable air in cities and villages, a = 0.27 [56]. Volumetric flow rate at 5 mm is then calculated using Eq. (8):

$$V = w \times h \times v_{5mm} \quad (8)$$

where w is the width (m) and h is the height (m) of air volume passing over the photocatalytic area (m). It can be noted that the closed volume of ISO reactor defines a different flow velocity gradient but the distribution calculated using Eq. (7) is considered to provide a close approximation to near surface (5 mm) wind velocities.

When tested against data acquired from a photocatalytic test site of Ref. [55], the model was not able to reproduce the measured effect of photocatalysis with the lab-measured ξ(NO) value for the photocatalyst (mixed in a cement mortar) of 0.023%. Fitting the measured trend in NO concentrations required an 'effective' photonic efficiency, ξ'(NO), of 0.005% (see SI testing model section). The most likely reason for the deviation is that the model predicts the concentration in the air volume up to a height of only 5 mm from the photocatalyst surface whereas the site measurement was obtained at a height of 2 m. Parameters controlled in the laboratory are mostly variable in the environment, i.e., humidity, light intensity (cloud cover), and other environmental parameters such as local airflow characteristics and competition for photocatalyst adsorption sites (e.g. from water, SOx and VOCs). All can be expected to influence measured NO concentrations, both C_i and C_d.

Nevertheless, it can be anticipated that these model outputs represent a source term data set which can be implemented in a fluid dynamics model to define the distribution of NO concentrations from the modelled 5 mm volume to more useful volumes of relevance to the public, i.e. up to 2–3 m.

The implications of this analyses underlines the significance of a high photonic efficiency. In the application of the source term model to the Copenhagen site, the effective photonic efficiency, ξ'(NO), of 0.005% required in an empirical fitting of the measured data is 22% of the laboratory based value. Applying the same factor to the aggregate-supported photocatalyst QST-6-N (i.e. the free-standing composite), with a ξ(NO) of 0.89%, would give a ξ'(NO), of 0.2%, a 40 times improvement in NO removal efficiency. However, the diffusion rates of NO into this remediated volume balanced against the production rates (from vehicle emissions and other sources), as well as humidity and competition influences must also be considered in extending the model to more practical air volumes on site.

4. Conclusions

In this study, various quartz-supported TiO_2 composites were prepared by coating with TiO_2 loadings varying from TiO_2/SiO_2 ratios of 0.16–0.61%. In these, Ti-O-Si chemical linkages were confirmed and TiO_2 was accumulated on the surface in multiple agglomerated layers. The Ti-O-Si/Si-O-Si linkage ratios, obtained from a quantitative treatment of FTIR spectra, remained constant despite the TiO_2 loading, indicating that the bonded interface saturated the SiO_2 surface. Durability assessments of the composites showed significant losses of TiO_2 (almost half) at the highest loading levels, whereas composites with lower loadings were stable due to the strength and short range influence of the chemical Ti−O−Si binding.

Photocatalytic performance was also dependent on loading; activity increased with TiO_2 content up to ca. 0.76% and nitrate selectivity increased across the loading range. This is strongly conditioned by the negative influence of the Ti−O−Si bond on selectivity and the effect of dilution as TiO_2 loading is increased. However, after washing to remove weakly bonded TiO_2, photocatalytic activity (ξ (NO)) is only reduced by 30% even though almost half of the TiO_2 has been lost (0.34% remaining) whereas selectivity is not significantly affected (Fig. 12).

The simulated cement environment has indicated an enhancement in nitrate selectivity. This may be associated with alkaline hydrolysis of the TiO_2 surface and/or to influencing the availability of surface physi/chemisorbed water reported to be important in the photocatalytic oxidation of NO_2 [35]. The deposition of $Ca(OH)_2$, which also positively influences selectivity, may be important in attracting surface water. $CaCO_3$ deposition is at the expense of $Ca(OH)_2$ and consequently, its positive effects are diluted.

A model is presented to illustrate the expected seasonal impact of the produced photocatalyst-support composites on near-surface air composition, based on their measured photonic efficiencies. The model is not yet suitable for predicting impacts on air quality but provides a basis for fluid dynamics modelling to provide more accurate predictions of concentration distribution arising from the balance between the remediated surface layer and NOx production in the higher zones. Despite the early stage of development, the model clearly highlights the importance of maximising photonic efficiency. The significant increase in ξ (NO) highlighted for the TiO_2-support composites compared with conventionally dispersed photocatalyst in cements is readily extrapolated to illustrate the impacts on near-surface remediation efficiencies.

Acknowledgements

Appendix A. Supplementary data

Supplementary data associated with this article can be found, in the online version, at http://dx.doi.org/10.1016/j.apcatb.2017.10.013.

References

[1] H.B. Singh, L.J. Salas, W. Viezee, Global distribution of peroxyacetyl nitrate, Nature 321 (1986) 588–591.

[2] EU, Directive 2001/81/EC of the European Parliament and of the Council of 23 October 2001 on National Emission Ceilings for Certain Atmospheric Pollutants, 2001.

[3] Department for Environment Food & Rural Affairs. https://uk-air.defra.gov.uk/latest/currentlevels?period=24.

[4] Y. Zhu, J. Zhang, J. Wang, W. Chen, Y. Han, C. Ye, Y. Li, J. Liu, L. Zeng, Y. Wu, X. Wang, W. Wang, J. Chen, T. Zhu, Distribution and sources of air pollutants in the North China Plain based on on-road mobile measurements, Atmos. Chem. Phys. 16 (2016) 12551–12565.

[5] London Average Air Quality Levels. https://data.london.gov.uk/dataset/london-average-air-quality-levels (Accessed 20 July 2017).

[6] G. Hüsken, M. Hunger, H.J.H. Brouwers, Experimental study of photocatalytic concrete products for air purification, Build. Environ. 44 (2009) 2463–2474.

[7] A. Fiore, G.C. Marano, P. Monaco, A. Morbi, Preliminary experimental study on the effects of surface-applied photocatalytic products on the durability of reinforced concrete, Constr. Build. Mater. 48 (2013) 137–143.

[8] E. Boonen, A. Beeldens, Photocatalytic roads: from lab tests to real scale applications, Eur. Transp. Res. Rev. 5 (2013) 79–89.

[9] A. Folli, C. Pade, T.B. Hansen, T. De Marco, D.E. Macphee, TiO_2 photocatalysis in cementitious systems: insights into self-cleaning and depollution chemistry, Cem. Concr. Res. 42 (2012) 539–548.

[10] F. Wang, L. Yang, G. Sun, L. Guan, S. Hu, The hierarchical porous structure of substrate enhanced photocatalytic activity of TiO_2/cementitious materials, Constr. Build. Mater. 64 (2014) 488–495.

[11] J. Chen, C.S. Poon, Photocatalytic cementitious materials: influence of the microstructure of cement paste on photocatalytic pollution degradation, Environ. Sci. Technol. 43 (2009) 8948–8952.

[12] M.M. Ballari, H.J.H. Brouwers, Full scale demonstration of air-purifying pavement, J. Hazard. Mater. 254–255 (2013) 406–414.

[13] M.J. Hanus, A.T. Harris, Nanotechnology innovations for the construction industry, Prog. Mater. Sci. 58 (2013) 1056–1102.

[14] F. Pacheco-Torgal, S. Jalali, Nanotechnology Advantages and drawbacks in the field of construction and building materials, Constr. Build. Mater. 25 (2011) 582–590.

[15] S.S. Lucas, V.M. Ferreira, J.L.B. de Aguiar, Incorporation of titanium dioxide nanoparticles in mortars – influence of microstructure in the hardened state properties and photocatalytic activity, Cem. Concr. Res. 43 (2013) 112–120.

[16] E. Jimenez-Relinque, J.R. Rodriguez-Garcia, A. Castillo, M. Castellote, Characteristics and efficiency of photocatalytic cementitious materials: type of binder, roughness and microstructure, Cem. Concr. Res. 71 (2015) 124–131.

[17] M.Z. Guo, T.C. Ling, C.S. Poon, Nano TiO_2 based architectural mortar for NO removal and bacteria inactivation: influence of coating and weathering conditions, Cem. Concr. Compos. 36 (2013) 101–108.

[18] R. Zouzelka, J. Rathousky, Photocatalytic abatement of NOx pollutants in the air using commercial functional coating with porous morphology, Appl. Catal. B: Environ. 217 (2017) 466–476.

[19] Picada-project, photocatalytic Innovative Coverings Applications for Depollution Assessment. http://www.picada-project.com/domino/SitePicada/Picada.nsf?OpenDataBase.

[20] R & D-project. http://www.light2cat.eu/.

[21] L. Cassar, Photocatalysis of cementitious materials: clean buildings and clean air, MRS Bull. 29 (2004) 328–331.

[22] L. Cassar, A. Beeldens, N. Pimpinelli, G.L. Guerrini, Photocatalysis of cementitious materials, in: P.B.a.L. Casssar (Ed.), International RILEM Symposium on Photocatalysis, Environment and Construction Materials – TDP 2007, RILEM Publications SARL, Italy, 2007, pp. 131–145.

[23] E. Boonen, A. Beeldens, Recent photocatalytic applications for air purification in Belgium, Coatings 4 (2014) 553–573.

[24] C.E. Bygott, J.E. Maltby, J.L. Stratton, R. McIntyre, Photocatalytic coatings for the construction industry, in: P.B.a.L. Casssar (Ed.), International RILEM Symposium on Photocatalysis, Environment and Construction Materials – TDP 2007, RILEM Publications SARL, Italy, 2007, pp. 251–258.

[25] C. Qian, L. Zhao, D. Fu, L. Li, R. Wang, Photocatalytic oxidation of nitrogen oxides by nano-TiO_2 immobilised on road surface materials, J. Chin. Ceram. Soc. 33 (2005) 422–427.

[26] D.E. Macphee, A. Folli, Photocatalytic concretes—the interface between photocatalysis and cement chemistry, Cem. Concr. Res. 85 (2016) 48–54.

[27] S. Karapati, T. Giannakopoulou, N. Todorova, N. Boukos, I. Papailias, D. Dimotikali, C. Trapalis, Novel 'Pickering' modified TiO_2 photocatalysts with high De-NOx efficiency, Catal. Today 287 (2017) 45–51.

[28] S. Karapati, T. Giannakopoulou, N. Todorova, N. Boukos, D. Dimotikali, C. Trapalis, Eco-efficient TiO_2 modification for air pollutants oxidation, Appl. Catal. B: Environ.

176–177 (2015) 578–585.

[29] F. Wang, L. Yang, H. Wang, H. Yu, Facile preparation of photocatalytic exposed aggregate concrete with highly efficient and stable catalytic performance, Chem. Eng. J. 264 (2015) 577–586.

[30] L. Yang, A. Hakki, F. Wang, D.E. Macphee, Different roles of water in photocatalytic DeNOx mechanisms on TiO_2: basis for engineering nitrate selectivity? ACS Appl. Mater. Interfaces 9 (2017) 17034–17041.

[31] J.Z. Bloh, A. Folli, D.E. Macphee, Photocatalytic NOx abatement: why the selectivity matters, RSC Adv. 4 (2014) 45726–45734.

[32] P.E. Morrow, An evaluation of recent NOx toxicity data and an attempt to derive an ambient air standard for NOx by established toxicological procedures, Environ. Res. 10 (1975) 92–112.

[33] S.M. Al-Alawi, S.A. Abdul-Wahab, C.S. Bakheit, Combining principal component regression and artificial neural networks for more accurate predictions of ground-level ozone, Environ. Model. Softw. 23 (2008) 396–403.

[34] W. Qiu, Y. Zheng, A comprehensive assessment of supported titania photocatalysts in a fluidized bed photoreactor: photocatalytic activity and adherence stability, Appl. Catal. B: Environ. 71 (2007) 151–162.

[35] N.V. Vagenas, A. Gatsouli, C.G. Kontoyannis, Quantitative analysis of synthetic calcium carbonate polymorphs using FT-IR spectroscopy, Talanta 59 (2003) 831–836.

[36] D.C.M. Dutoit, M. Schneider, R. Hutter, A. Baiker, Titania–silica mixed oxides, J. Catal. 161 (1996) 651–658.

[37] R.L. Pozzo, J.L. Giombi, M.A. Baltanás, A.E. Cassano, The performance in a fluidized bed reactor of photocatalysts immobilized onto inert supports, Catal. Today 62 (2000) 175–187.

[38] H. Kisch, D. Bahnemann, Best practice in photocatalysis: comparing rates or apparent quantum yields? J. Phys. Chem. Lett. 6 (2015) 1907–1910.

[39] J. Tokarský, V. Matějka, L. Neuwirthová, J. Vontorová, K. Mamulová Kutláková, J. Kukutschová, P. Čapková, A low-cost photoactive composite quartz sand/TiO_2, Chem. Eng. J. 222 (2013) 488–497.

[40] L. Wu, Y. Zhou, W. Nie, L. Song, P. Chen, Synthesis of highly monodispersed teardrop-shaped core–shell SiO_2/TiO_2 nanoparticles and their photocatalytic activities, Appl. Surf. Sci. 351 (2015) 320–326.

[41] L. Yuan, C. Han, M. Pagliaro, Y.-J. Xu, Origin of enhancing the photocatalytic performance of TiO_2 for artificial photoreduction of CO_2 through a SiO_2 coating strategy, J. Phys. Chem. C 120 (2016) 265–273.

[42] M. Fujishima, H. Takatori, H. Tada, Interfacial chemical bonding effect on the photocatalytic activity of TiO_2–SiO_2 nanocoupling systems, J. Colloid Interface Sci. 361 (2011) 628–631.

[43] M.A. Holland, D.M. Pickup, G. Mountjoy, E.S. Tsang, G.W. Wallidge, R.J. Newport, M.E. Smith, Synthesis, characterisation and performance of (TiO_2)0.18 (SiO_2)0.82 xerogel catalysts, J. Mater. Chem. 10 (2000) 2495–2501.

[44] T.V. Nguyen, S. Kim, O.B. Yang, Water decomposition on TiO_2–SiO_2 and RuS_2/TiO_2–SiO_2 photocatalysts: the effect of electronic characteristics, Catal. Commun. 5 (2004) 59–62.

[45] A. Hakki, L. Yang, F. Wang, D. Macphee, Effect of interfacial chemical bonding in TiO_2-SiO_2 composites on their photocatalytic NOx abatement performance, J. Visual. Exp. JoVE (2017).

[46] Z. Lu, Q. Wang, R. Yin, B. Chen, Z. Li, A novel TiO_2/foam cement composite with enhanced photodegradation of methyl blue, Constr. Build. Mater. 129 (2016) 159–162.

[47] M.Z. Guo, A. Maury-Ramirez, C.S. Poon, Self-cleaning ability of titanium dioxide clear paint coated architectural mortar and its potential in field application, J. Clean. Prod. 112 (2016) 3583–3588.

[48] E. Bocci, L. Riderelli, G. Fava, M. Bocci, Durability of NO oxidation effectiveness of pavement surfaces treated with photocatalytic titanium dioxide, Arab. J. Sci. Eng. 41 (2016) 4827–4833.

[49] C.L. Bianchi, C. Pirola, F. Galli, G. Cerrato, S. Morandi, V. Capucci, Pigmentary TiO_2: A challenge for its use as photocatalyst in NOx air purification, Chem. Eng. J. 261 (2015) 76–82.

[50] N. Todorova, T. Giannakopoulou, S. Karapati, D. Petridis, T. Vaimakis, C. Trapalis, Composite TiO_2/clays materials for photocatalytic NOx oxidation, Appl. Surf. Sci. 319 (2014) 113–120.

[51] S. Kamaruddin, D. Stephan, Quartz–titania composites for the photocatalytical modification of construction materials, Cem. Concr. Compos. 36 (2013) 109–115.

[52] A. Folli, I. Pochard, A. Nonat, U.H. Jakobsen, A.M. Shepherd, D.E. Macphee, Engineering photocatalytic cements: understanding TiO_2 surface chemistry to control and modulate photocatalytic performances, J. Am. Ceram. Soc. 93 (2010) 3360–3369.

[53] J. Chen, C.S. Poon, Photocatalytic construction and building materials: from fundamentals to applications, Build. Environ. 44 (2009) 1899–1906.

[54] L. Yang, F. Wang, D. Du, P. Liu, W. Zhang, S. Hu, Enhanced photocatalytic efficiency and long-term performance of TiO_2 in cementitious materials by activated zeolite fly ash bead carrier, Constr. Build. Mater. 126 (2016) 886–893.

[55] A. Folli, J.Z. Bloh, M. Strøm, T. Pilegaard Madsen, T. Henriksen, D.E. Macphee, Efficiency of Solar-Light-Driven TiO_2 Photocatalysis at Different Latitudes and Seasons. Where and When Does TiO_2 Really Work? J. Phys. Chem Lett. 5 (2014) 830–832.

[56] M. Kaltschmitt, W. Streicher, A. Wiese, Renewable Energy; –Technology, Economics and Environment, Springer, Berlin Heidelberg, New York, 2007 (pp. p55.).